# Thermolytic Reverse Electrodialysis Heat Engine:

# model development, integration and performance analysis

F. Giacalone[a], F. Vassallo[a], L. Griffin[a,b], M.C. Ferrari[b], G. Micale[a], F. Scargiali[a]*, A.

Tamburini[a], A.Cipollina[a]

[a]Dipartimento dell'Innovazione Industriale e Digitale (DIID), Università degli Studi di

Palermo (UNIPA), viale delle Scienze Ed.6, 90128 Palermo, Italy.

[b]School of Engineering, Institute for Materials and Processes, The University of Edinburgh,

The King's Buildings, Edinburgh EH9 3JL, UK

*e–mail: francesca.scargiali@unipa.it,

## ABSTRACT

Salinity gradient heat engines represent an innovative and promising way to convert low-grade heat into electricity by employing salinity gradient technology in a closed-loop configuration. Among the aqueous solutions which can be used as working fluid, ammonium bicarbonate-water solutions appear very promising due to their capability to decompose at low temperature. In this work, an experimentally validated model for a reverse electrodialysis heat engine fed with ammonium bicarbonate-water solutions was developed. The model consists of two validated sub-models purposely integrated, one for the reverse electrodialysis unit and the other for the stripping/absorption regeneration unit. The impact of using current commercial membranes and future enhanced membranes on the efficiency of the system was evaluated, along with the effect of operating and design parameters through sensitivity analyses. Results

26     indicated that exergy efficiency up to 8.5% may be obtained by considering enhanced future

27     membranes and multi-column regeneration units.

28     **KEYWORDS**

29     Thermolytic salts, Salinity Gradient Heat Engine, Regeneration unit, Reverse Electrodialysis,

30     Ammonium Bicarbonate solutions, Waste Heat Recovery.

31     **1   INTRODUCTION**

32     The increasing demand of energy due to population and industrial growth is an open issue

33     nowadays while increasing attention is paid to the sustainable production of energy. In this

34     scenario of opposing challenges, interest towards non-conventional or under-used resources is

35     rapidly increasing. Low-grade heat coming from geothermal sources, sun or industrial activities

36     is a resource being as abundant as under-used, because no technology has been proposed so far

37     to convert efficiently such heat into electricity [1]. The potential availability of waste heat in

38     the EU industrial sector has been estimated at about 304.13 TWh/year, mainly represented by

39     waste heat at temperatures in the range 100-200 °C (40% of the total) [2].

40     Salinity gradient power heat engines (SGP HEs) have been recently proposed as a viable

41     process to convert low-grade heat into electricity [3]. A SGP HE system consists of two main

42     units: (i) a power generation unit based on salinity gradient power process, where the

43     concentration difference between two salt solutions is exploited to produce electricity, and (ii)

44     a regeneration unit where low-grade heat is used to restore the original concentration values of

45     the solutions exiting from the power generation unit. The restoring of the two solutions can be

46     achieved by means of different strategies, e.g. (i) solvent extraction and (ii) salt extraction [1].

47     In solvent extraction, the salt exchanged within the power unit is rebalanced by adding a part

48     of the exhausted dilute stream to the exhausted concentrate stream. Then, the resulting solution

49  is fed to the regeneration unit where the solvent is recovered by a thermal separation process

50  (e.g. multi-effect distillation, membrane distillation) and transferred to the dilute solution.

51   In salt extraction, the exhausted dilute solution is fed to the regenerative unit where salt is

52  recovered by using low-grade heat and transferred again to the concentrate solution.

53  Rebalancing of the solvent is eventually carried-out to restore the solvent amount in the two

54  streams.

55   The concept of SGP HE was proposed for the first time by Loeb more than forty years ago,

56  for both pressure retarded osmosis (PRO) [4] and reverse electrodialysis (RED) [5] heat

57  engines. Only in recent years, the growing improvement and the decreasing cost of the

58  membranes used in SGP technologies are boosting research interest on this topic.

59   Compared to open loop SGP technologies, SGP HEs give the great advantage of allowing

60  artificial streams in a closed circuit along with the adoption of any solute-solvent couple. This

61  advantage avoids the geographical constraint of limited availability of streams at different

62  salinity and, more importantly, allows to achieve higher performances as the salinity gradient

63  can be suitably chosen and tuned.

64   Several works have been already devoted to different SGP HE configurations. In particular,

65  both solvent and salt extraction strategies have been studied. As concerns the solvent extraction

66  strategy, some works investigated the performance of SGP HEs with different regeneration

67  technologies for the case of sodium chloride (NaCl) - water solutions. Lin et al. [6] carried out

68  a theoretical study on a heat engine, in which PRO (an osmotic heat engine, OHE) was coupled

69  with a membrane distillation (MD) regeneration unit. Long et al. [7] performed a parametric

70  study on a hybrid RED-MD system. The results showed, in best conditions, a maximum exergy

71  efficiency of about 10%. Similarly, Micari et al. [8] performed a theoretical analysis for the

72  design of a RED-MD prototype considering the behaviour of real units and providing

73  perspectives. An integrated system can provide an exergy efficiency equal to 2.3%, while

74 considering technological improvements on both units, an exergy efficiency of 16.5% can be

75 achieved.

76  Recently, other studies reported theoretical analysis concerning the performance of a heat

77 engine coupling a RED unit with a multi effect distillation system (MED). In particular, Hu et

78 al. [9] reported a maximum exergy efficiency of about 5%, coupling a RED unit with a MED

79 of 10 effects fed with low-grade heat at 95 °C. Palenzuela et al. [10] investigated the impact of

80 membrane properties and operating conditions on the integrated system. They reported an

81 exergy efficiency around 7% for the case of real membranes using low-grade heat at 100°C,

82 and up to almost 31% for the case of ideal membranes.

83 Other authors studied the impact of different solute-solvent couples. For instance, Shaulsky et

84 al. [11] proposed an OHE fed by lithium chloride (LiCl) - methanol solutions. Marino et al.

85 [12] proposed an electrochemical cell coupled to a distiller using zinc chloride ($ZnCl_2$) - water

86 solutions as working solution. Hickenbottom et al. [13] experimentally investigated the impact

87 of using different salt solutions as possible working fluid of a PRO-MD HE. Their findings

88 indicate calcium chloride as the most promising salt for both PRO and MD processes. Carati et

89 al. [14] presented a theoretical analysis on SGP HE, focusing on the effect of different salt-

90 water solutions, namely NaCl, $ZnCl_2$ and sodium hydroxide (NaOH) water solutions, on the

91 performance of a unit constituted of a distiller and an ideal SGP unit. Similarly, Giacalone et

92 al. [15] performed a theoretical analysis concerning the influence of different salt-water

93 solutions, namely NaCl, LiCl, potassium chloride (KCl), potassium acetate ($KCH_3CO_2$),

94 caesium acetate ($CsCH_3CO_2$) and sodium acetate ($NaCH_3CO_2$) water solutions, on the

95 performance of SGP HEs consisting of single and multi-stage regeneration units. Micari et al.

96 [16] experimentally investigated the performance of a RED unit fed by aqueous solutions of

97 binary salt mixtures.

98   Concerning the salt extraction strategy, the use of aqueous solutions of thermolytic salts has

99   been considered so far as one of the most promising solvent-solute couples. Thermolytic salts

100  have the capability of decomposing into gaseous compounds at the low temperatures at which

101  waste heat is available (60-100°C). Thus, the thermolytic salt of the dilute solution is

102  decomposed into gaseous compounds, subsequently it is adsorbed into the concentrate solution

103  (salt extraction strategy). Ammonium bicarbonate ($NH_4HCO_3$) is the most commonly used

104  thermolytic salts in such applications as it is able to decompose into carbon dioxide and

105  ammonia above 50-60°C [4]. About ten years ago, McGinnis et al. [17] proposed an OHE where

106  PRO is coupled with a distillation column fed with $NH_4HCO_3$ solutions. They found that the

107  high thermal energy consumption affects the global energetic efficiency. Similarly, Luo et al.

108  [18] and Cusick et al. [19] proposed a RED unit and a microbial RED unit, respectively, fed

109  with $NH_4HCO_3$ solution and coupled to a distillation column.

110  In recent years, several researchers have focused their attention on the performance of RED

111  units fed by $NH_4HCO_3$ aqueous solutions. In particular, Kwon et al. [20] presented an

112  experimental analysis, reporting a maximum power density (1.54 $W/m^2_{cell\ pair}$), doubling that

113  achieved by Luo et al. [18]. Similarly, Bevacqua et al. [21] presented an experimental

114  investigation aimed to maximize the performance of a laboratory RED unit fed by $NH_4HCO_3$,

115  recording the highest power density achieved so far in RED units fed by aqueous solutions of

116  $NH_4HCO_3$ (i.e., 2.42 $W/m^2_{cell\ pair}$). In 2017, Kim et al. [22] proposed a validated model to predict

117  the performance of a RED unit fed by $NH_4HCO_3$ solutions.

118  A first preliminary attempt to perform an accurate analysis of the whole heat engine including

119  also the regeneration step was performed for the first time by Bevacqua et al. [23], who carried

120  out a modelling analysis on a RED HE system operating with aqueous solution of $NH_4HCO_3$.

121  The proposed HE consists of a RED unit and a thermal regeneration unit including an air

122  stripping column to restore the initial salinity gradient. The highest energy efficiency reported

123  was equal to 22%.

124  Notwithstanding the growing interest on RED HEs only few theoretical studies have been

125  carried out so far on the whole system. Most of them were focused on the RED unit without

126  analysing the regeneration unit and the integrated system performances.

127  In a previous work [24], a validated RED model was developed to perform an exergy analysis of

128  RED units fed with NaCl-water solutions. In the present work, an experimentally validated

129  model of an integrated RED HE fed by thermolytic $NH_4HCO_3$ solutions (t-RED HE) is

130  presented. The proposed t-RED HE consists of a RED unit coupled to a vapour stripping column

131  for the stripping of the salts, and an absorption process where the gases are reabsorbed. The

132  model comes from the integration of two sub-models: (i) the RED unit model, obtained by

133  upgrading the previous RED model [23]; (ii) the stripping/absorption regeneration units,

134  purposely developed in Aspen plus$^{®}$. Sensitivity analyses were carried out in order to evaluate

135  the performance of the RED HE as a whole. The effect of operating and design parameters on

136  the thermal and exergy efficiencies of the system was investigated. Furthermore, a perspective

137  analysis is presented assuming enhanced properties of the ionic exchange membranes (IEMs).

138  **2  METHODS**

139  The thermolytic RED HE is composed of two units: (i) a RED unit where power is produced

140  exploiting the salinity gradient between $NH_4HCO_3$ solutions as the power generation unit; (ii)

141  a thermal regeneration unit where low-grade waste heat is used to restore the initial conditions

142  of the two streams exiting the RED unit, as the regeneration unit. A schematic representation

143  of the entire t-RED HE is reported in Figure 1.

144
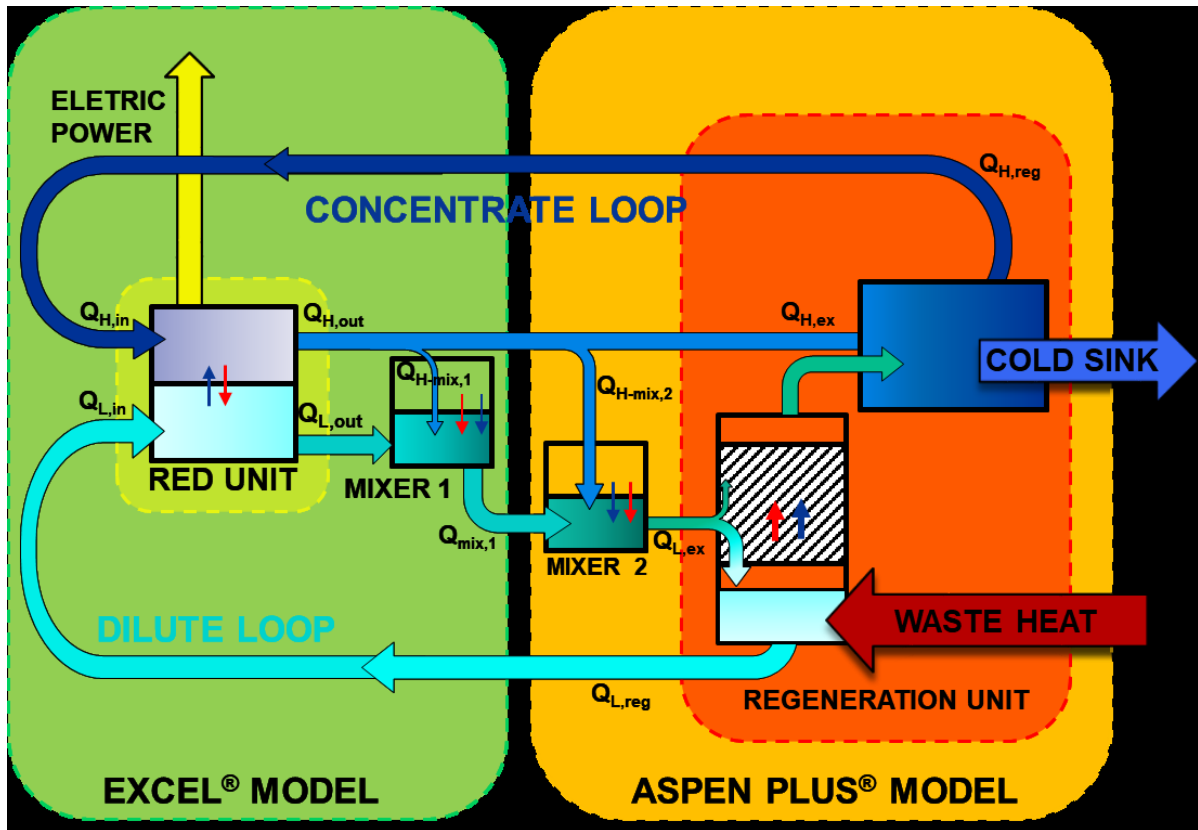
**Figure 1** *System scheme used in the exergy analysis. Blue arrows indicate the direction of water fluxes while red arrows indicate the direction of salt fluxes.*

The two $NH_4HCO_3$ solutions, i.e., the dilute and the concentrate, are pumped to the RED unit to convert their salinity gradient into electricity. During the process, part of the salt content in the concentrate solution is transferred to the dilute solution, while water is transferred from dilute to concentrate due to the osmotic flux. In order to restore the initial conditions of the two streams in the regeneration unit, both salt and water transport have to be promoted in the opposite direction.

After exiting from the RED stack, the dilute solution is mixed with a small amount of the concentrate stream in mixer 1, in order to restore the water content in the dilute stream. Notably, this step is extremely important in order to restore the flow rate of the two streams since the system operates in a closed loop. The second mixer (mixer 2) fulfils a similar task, restoring the amount of water consumed in the stripping process due to the partial vaporization of the

159    dilute stream. In practical applications, the water-restoring step can be carried out in one mixer

160    only. Here, two different mixers are considered because the two sub-models (i.e., one for the

161    RED unit and one for the regeneration unit) are developed in different software and each of

162    them includes a mixer. The resulting stream from mixer 2 is fed to the vapour stripping column

163    operating in vacuum conditions. Here, the $NH_4HCO_3$ is decomposed into ammonia and carbon

164    dioxide, which are stripped by means of a vapour stream produced from the partial vaporization

165    of the solution in the reboiler. Low-grade waste heat (T≤ 100 °C) is used as an energy source.

166    The stripped gasses are absorbed again into the concentrate solution through a low temperature

167    (25 °C) absorption process. The two regenerated solutions are finally sent back to the stack

168    where their difference in chemical potential is used again to generate electricity.

169    The whole model consists of two experimentally validated sub-models (Fig. 1):

170        (i)    The RED unit model, including mixer 1, implemented in Excel®;

171        (ii)    The regeneration unit model, including mixer 2, implemented in Aspen plus®.

172    A description of the model is reported in the following sections.

173    **2.1    Reverse electrodialysis model**

174    The modelling approach is similar to that reported in a previous work [24], where a validated RED

175    model is presented and used to perform an exergy analysis of RED units fed by NaCl-water

176    solutions. In particular, the concentration and flow rate variations along the channels are

177    accounted for by adopting a mono-dimensional approach. The unit, consisting of a given

178    number of cell pairs (i.e., $N_{cp}$), is discretized in $N_k$ calculation elements along the main flow

179    direction. Each calculation element represents a branch of an equivalent circuit, where passive

180    (i.e., resistances) and active (i.e., generator) elements are present. Full details are reported in

181    [24]. The electric voltage ($E_{cell}$) produced in the generic $k^{th}$ element of a cell pair is calculated

182    according to the following equation:

8

183
$$E_{cell}(k) = 2\alpha_{av}(k)\frac{RT}{zF}\ln\left(\frac{m_H(k)\cdot\gamma_H(k)}{m_L(k)\cdot\gamma_L(k)}\right)$$
(1)

184 where $\alpha_{av}$ is the average membranes permselectivity, $\gamma_H$ and $\gamma_L$ are the activity coefficients of

185 the two solutions, $m_H$ and $m_L$ are the solutions molality, $z$ is the z is the valence of the ions, $F$

186 is the Faraday's constant, $R$ is the universal gas constant and $T$ is the absolute temperature ($T=$

187 298 K).

188 The resistance of the $k^{th}$ element of the cell pair ($R_{cell}$) is given by the sum of 4 resistances in

189 series:

190
$$R_{cell}(k) = \left[R_H(k) + R_L(k) + R_{CEM}(k) + R_{AEM}(k)\right]\frac{1}{\Delta x \cdot b}$$
(2)

191 where $R_{CEM}$ and $R_{AEM}$ are the membrane resistances, $R_H$ and $R_L$ the electrical resistances of the

192 solutions flowing in the two channels, $\Delta x$ is the length of the calculation element and $b$ is the

193 membrane width. Thus, the electric current ($i$) circulating in the $k^{th}$ branch is computed

194 according to:

195
$$i(k) = \frac{N_{cp}E_{cell}(k) - (E_{stack} + R_{blank}I_{stack})}{N_{cp}R_{cell}(k)}$$
(3)

196 where $E_{stack}$ is the electric voltage generated by the RED unit and $R_{blank}$ is the resistance of the

197 electrodic compartments, which is negligible for high cell pairs number (e.g. larger than 100

198 cell pairs). The electric current circulating on the external load ($I_{stack}$) is the sum of the currents

199 produced in the $k^{th}$ branch (Kirchhoff's junction rule).

200
$$I_{stack} = \sum_k i(k)$$
(4)

201 The closing equation is obtained by the Ohm's law on the external load (Eq. 5).

202
$$E_{stack} = R_E \cdot I_{stack}$$
(5)

203 where $R_E$ is the resistance of the external load. The gross power ($P_{RED}$) and the gross power

204 density ($P_d$) are calculated as follows:

$$205 \qquad\qquad P_{RED} = E_{stack} \cdot I_{stack} \qquad\qquad (6)$$

$$206 \qquad\qquad P_d = \frac{P_{RED}}{N_{cp} A_{cp}} \qquad\qquad (7)$$

207  where $A_{cp}$ is the area of a cell pair.

208  In order to compute the maximum power density ($P_{d,max}$), the value of external load resistance

209  is optimized and is typically set to the same value of the stack internal resistance [8].

210  The model also considers the water and salt fluxes across the membranes. The model does not

211  account for pressure drops along the channel, thus only gross power and gross power density

212  values are reported. Pressure drops are mainly related to the geometry of stack configuration,

213  and generally account for 10 to 20% . The complete description of the model is reported in [24]

214  for the case on NaCl-water solutions.

215  In order to account for the variation of the properties of $NH_4HCO_3$ aqueous solution along the

216  channels, molality-dependent correlations are used. In particular:

217        (i)     the activity and osmotic coefficients of $NH_4HCO_3$-water solutions are estimated

218                through Pitzer's model [25];

219        (ii)    the densities of the solutions are estimated as a linear function of the molar

220                concentration using literature data to obtain the fitting coefficients [26];

221        (iii)   the salt-solution conductivity is estimated using the Jone and Dole's equation with

222                experimentally fitting parameters [27].

223  All the relevant equations to estimate the solutions properties and graphical comparisons between

224  fitting equations and experimental literature data are reported in the Appendix.

225  Membrane resistance and permselectivity variation along the stack are taken into consideration by

226  adopting concentration-dependent correlations provided by the membrane manufacturer, while

227  constant values for water permeability and salt diffusivity were considered (see Table 1 for

228  reference values). In particular, relevant equations for permselectivity versus concentrate

229    concentration and membrane electrical resistance versus dilute concentration are reported in the

230    following (eqs. 8-9):

231 
$$\alpha_{av} = 0.8924 \cdot C_H^{-0.069} \tag{8}$$

232 
$$R_{IEM,av} = 2.027 \cdot 10^{-4} \cdot C_L^{-0.236} \tag{9}$$

233    The correlations provide the values of the permselectivity and the electrical resistance ($R_{IEM,av}$) as

234    an average for both the anionic and the cationic exchange membranes.

235    Simulations were performed considering a RED unit consisting of 1000 cell pairs (cps) with

236    membrane area of 0.5 x 0.5 m$^2$ and spacers of 0.155 mm. Two different scenarios were analysed:

237    (i) a current scenario in which the RED unit is equipped with current membranes (Fujifilm

238    membranes); (ii) a future scenario in which future membranes with enhanced properties are

239    adopted (see Table 1). The enhancement in the case of future membranes is aimed at decreasing

240    the membrane resistance, the water and salt permeability, while increasing the permselectivity

241    [24]. For the case of NaCl aqueous solutions, the properties of future membranes are not far from

242    those of currently available membranes, as reported in [28] and described in [8].

243    **Table 1.** *Current and future membrane properties adopted in the analysis.*

| Properties | Current | Future |
|---|---|---|
| Permselectivity [%] | 85.1[*] | 95[**] |
| Resistance [Ω·m$^2$] | 6.01 10$^{-04}$[*] | 1.50 10$^{-04}$[*] |
| Water Permeability [ml/(bar·h·m$^2$)] | 6[**] | 1.5[**] |
| Salt diffusivity [m$^2$/s] | 4.5 10$^{-12}$[**] | 1.13 10$^{-12}$[**] |

244    [*]*reference concentration of 2 M-0.01 M NH$_4$HCO$_3$ water solutions. Property functions of solutions concentration*

245    [**]*assumed constant in the whole range of concentrations*

246

247    The model is closed by trivial global and salt mass balances in mixer 1. These are reported in

248    eqs. 10-11.

$$Q_{mix1} \cdot \rho_{mix1} = Q_{L,out} \cdot \rho_{L,out} + Q_{H-mix1} \cdot \rho_{H-mix1} \tag{10}$$

$$Q_{mix1} \cdot C_{mix1} = Q_{L,out} \cdot C_{L,out} + Q_{H-mix1} \cdot C_{H,out} \tag{11}$$

where $Q_i$, $\rho_i$ and $C_i$ are the volumetric flow rate, density and concentration of the $i^{th}$ generic stream, respectively. The subscripts *L,out*, *mix1* and H-*mix1* refer to the dilute stream exiting from the RED unit, the stream exiting from the mixer 1 and the part of the concentrate stream exiting from the RED unit added in the mixer, respectively. The $Q_{H-mix1}$ is evaluated from the water mass balance of the concentrate in the RED unit

$$Q_{H-mix1} = \frac{\left[ Q_{H,in}(\rho_{H,in} - C_{H,in}MW_s) - Q_{H,out}(\rho_{H,out} - C_{H,out}MW_s) \right]}{\rho_{H,out} - C_{H,out}MW_s} \tag{12}$$

where $MW_s$ is the molecular weight of $NH_4HCO_3$. Subscripts *in* and *out* refer to the inlet and outlet streams in the RED unit.

### 2.1.1   Reverse electrodialysis model validation

The RED model was validated by comparison with experimental results. Figure 2a and 2b show the trend of experimental and modelling stack voltage ($E_{stack}$) and power ($P_{RED}$) for two different salinity gradients (i.e., 0.6 M-0.05 M and 1.6 M-0.05 M) as function of the $I_{stack}$ and the $E_{stack}$, respectively, for a RED unit consisting of 50 cell pairs 0.1 x 0.4 m$^2$ provided by 0.155 mm spacers and considering solution velocities equal to 0.5 cm/s.

Model predictions fit very well with experimental trends, thus indicating the reliability of the model in the range of conditions investigated. The model was further validated considering different salt-water solutions, velocities, concentration and stack geometries, giving always a good agreement [24].
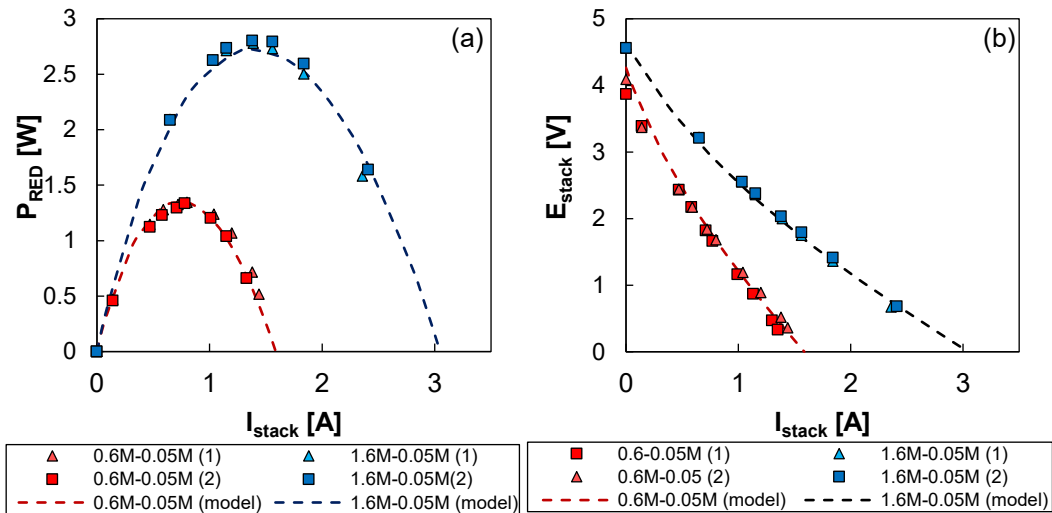
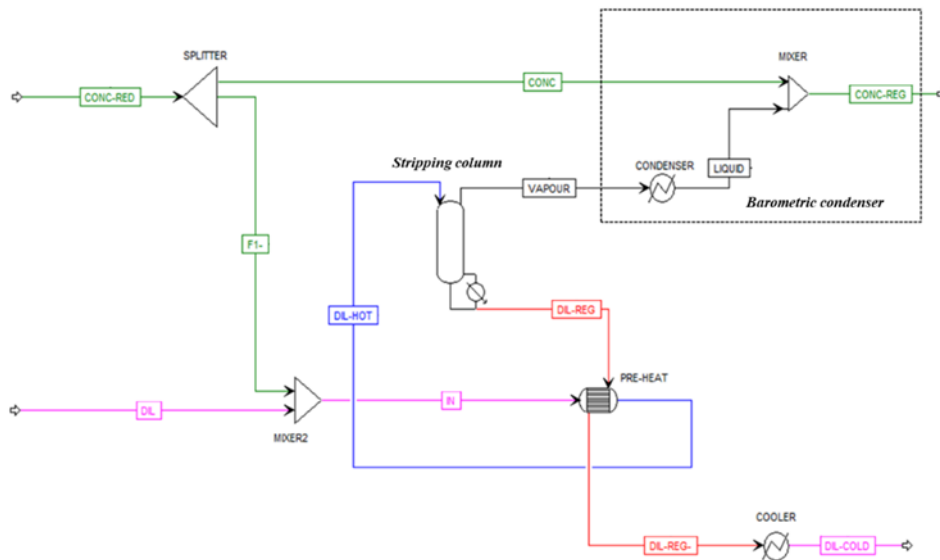**Figure 2.** *Power versus electrical current (a) and electrical potential versus current (b) in a RED unit fed by NH₄HCO₃ solutions (0.6 M-0.05 M and 1.6 M-0.05 M) at 0.5 cm/s. RED unit 50 cell pairs 0.1 x 0.4 m².*

## 2.2 Regeneration unit model

The regeneration unit of the thermolytic RED HE was modelled on Aspen plus®. The Aspen flow sheet of the process is reported in Figure 3.



**Figure 3.** *Aspen flow sheet of the regeneration process.*

The components and chemical equilibrium reactions involved in NH₄HCO₃-water solutions were described by adopting a multi-model approach. In fact, while the solution properties of

280  the liquid streams are evaluated adopting the *OLI*® property method, the behaviour of the

281  columns was modelled using the electrolyte non random two liquid Redlich-Kwong (E-NRTL-

282  RK) property method. The behaviour of the stripping column (Stripper) was modelled using a

283  *Rad-Frac* model, which provides rigorous methods for design of multistage separations, such

284  as distillation, absorption, and stripping processes. The model performs simulation, sizing, and

285  rating of tray or packed columns. The stripping column was set in rate-based mode in order to

286  take into account the heat/mass transfer, thermodynamic, hydrodynamic and chemical reaction

287  features. The absorption process was modelled as a mixer and a condenser (Absorber). Mixer

288  2 is used to restoring the amount of water lost in the dilute solution due to the vaporization

289  within the stripping column.

290  Concerning the barometric condenser, the cooling stream temperature was assumed equal to

291  20 °C while the outlet hot stream temperature was set to 25° C. The temperature of the waste

292  heat ($T_{waste-heat}$) that is used as hot utility in the stripping unit reboiler was assumed equal to 80 °C

293  while the boiling temperature is set to 75 °C.

294  Setting the chemical and physical properties of the inlet streams and the operating conditions

295  of the main equipment, the simulator computes the properties of outlet streams and evaluates

296  the thermal power consumption (TPC) to achieve a desired separation.

297  The operating and geometrical properties of the column were set as follows:

298  • Raschig rings of 15 mm were adopted as packing material;

299  • a design factor of 70% approach to flooding was chosen to compute the column diameter.

300  • column height was set equal to 2 m.

301  A thermal integration heat-exchanger (pre-heater) is used to recover part of the heat stored in

302  the dilute regenerated solution exiting from the reboiler by preheating the solution fed to the

303  vapour stripping column.

304     The concentration and flow rate of the resulting stream exiting from mixer 1 are the input of the

305     Aspen plus® regeneration model.

306     The mass balances for mixer 2 are implemented in the Aspen model flow sheet. The amount of

307     concentrate solution added to the dilute stream for rebalancing the water content due to the

308     generation of the stripping vapour is evaluated using the *design spec* tool of Aspen plus®. This tool

309     operates as a goal seek with the aim to compute the fraction of the concentrate stream to be added

310     to the dilute in order to balance the water lost in the stripping process. The thermal power required

311     for the separation is thus calculated by using a second *design spec* (operating in parallel to the

312     previous), which adjusts the value of the thermal power in order to get the desired concentration

313     of the regenerated dilute solution.

314     **2.2.1    Stripping unit model validation**

315     The regeneration unit model was validated comparing experimental results of a purposely-made

316     vapour stripping column with Aspen plus® model predictions. The experimental stripping column

317     consists of a structured packed column with a height of 1.6 m and an internal diameter of 5 cm.

318     The packing material is the Koch-Glitsch® FLEXIPAC 700Y. Figure 4 shows the trend of

319     experimental conductivities of the two regenerated solutions as a function of the dilute inlet

320     concentration (ranging from 0.2 M to 0.6 M) and the thermal power consumption (ranging from

321     700 W to 1000 W). The dilute inlet flow rate (i.e., 0.215 l/min) and the regeneration temperature

322     (i.e., between 70-80 °C) were kept constant. A reasonable agreement between experimental

323     results and model predictions was found with a maximum error of about 10% in the case of an

324     inlet concentration equal to 0.6 M .

325
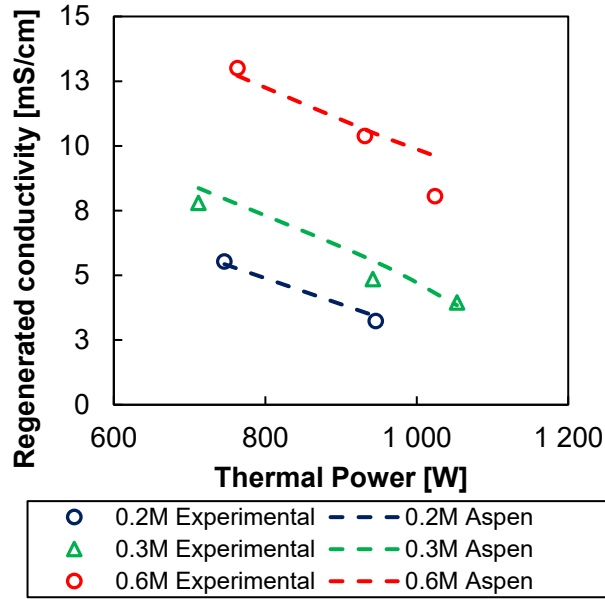
*Figure 4.* *Comparison of experimental measurements of regenerated solutions conductivity and model predictions as a function of the heat provided to the reboiler and of the inlet molarity of the solutions.*

## 2.3    Thermal and exergy efficiencies

The thermal efficiency ($\eta_{th}$) of the t-RED HE is defined as:

$$\eta_{th} = \frac{P_{RED}}{TPC} \tag{13}$$

The maximum achievable thermal efficiency is equal to the Carnot efficiency ($\eta_C$) evaluated at $T_{HOT} = 353$ K (maximum temperature) and $T_{COLD} = 293$ K (minimum temperature):

$$\eta_C = 1 - \frac{T_{COLD}}{T_{HOT}} \tag{14}$$

Finally, the exergy efficiency ($\eta_{ex}$) of the t-RED HE is the ratio between the energy efficiency and the Carnot efficiency. This parameter has been proposed as the most appropriate to compare different heat engines [29].

$$\eta_{ex} = \frac{\eta_{th}}{\eta_C} \tag{15}$$

16

339  It is worth noting that the efficiencies reported in the following do not take into account the

340  electric power consumption due to the pumping of the fluids. The pumping energy is generally

341  strongly affected by RED and regeneration units design. In the present case, the pumping power

342  can be considered as a fraction of the total power output in the range of 10-50%.

343  The above efficiencies are used along with the power density and the specific thermal

344  consumption as performance parameters in the sensitivity analysis reported in the following.

345  **3    RESULTS AND DISCUSSION**

346  The above mentioned sensitivity analyses were carried out in order to investigate the effect of

347  flow rate and concentration of the two solutions fed into the RED unit on the performance of

348  the integrated system for both current and future scenarios. Finally, the effect of using a multi-

349  stage regeneration unit was analysed.

350  **3.1      Influence of inlet concentration on the system performance**

351  The first sensitivity analyses show the effect of the solution concentration on the main

352  performance parameters of the t-RED HE considering a RED unit consisting of 1000 cell pairs

353  0.5x0.5 m$^2$. For the first analysis, the inlet velocity of the two solutions within the spacer-filled

354  channels was set to 1cm/s (i.e., typical value in RED operations).

355  The influence of the RED inlet concentration on $P_{d,max}$, is reported in Figure 5. As expected, the

356  higher the salinity gradient between the two solutions, the higher the power density obtainable

357  from the unit. As a matter of fact, when long stacks or large residence times are considered as

358  in the present case, the detrimental effect due to the dilute solution resistance becomes less

359  important. Conversely, if laboratory units (i.e., short stacks) or low residence times for the dilute

360  solutions are considered, then the dilute solution resistance is the controlling factor affecting

361  the power density. In the case of current membranes, the highest $P_{d,max}$ is equal to 2 W/m$^2$ while

17

362  in the case of future membranes it is equal to 4.25 W/m$^2$. The doubling in power density shifting

363  from current to future membrane is due to the reduction of the irreversible phenomena occurring

364  in the RED unit and responsible for the reduction of the available salinity gradient [24].
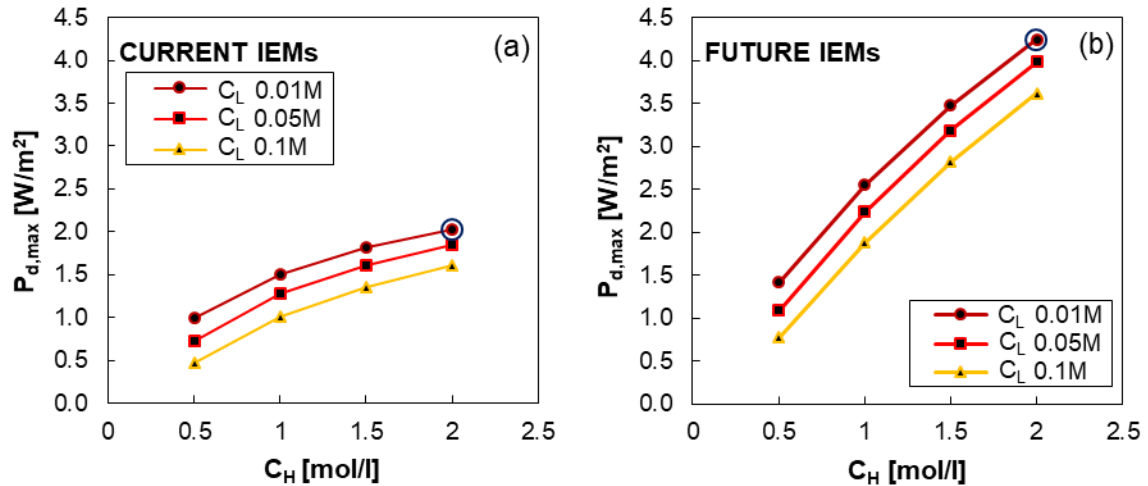
365



366  ***Figure 5.*** *Effect of inlet concentrations on P$_{d,max}$ of the RED unit for current (a) and future (b)*

367  *scenarios. RED unit 1000 cell pairs 0.5x0.5 m$^2$, inlet velocities equal to 1 cm/s. Blue circle is used to*

368  *highlight the best performance conditions.*

369  The effect of RED inlet concentration on the thermal power consumption of the vapour

370  stripping column is reported in Figure 6a and 6b for current and future membranes, respectively.

371  The higher the power generated in the RED unit, the higher is the salinity gradient consumed,

372  and therefore, the higher the thermal power consumption of the stripping column. The lowest

373  TPC values (around 160 kW) are obtained for the smaller salinity gradient considered (0.5 M-

374  0.1 M). Similar thermal energy consumptions are obtained for the two scenarios, i.e., current

375  and future (fig. 6), due to the effect of mixer 1. It should be observed that the two solutions

376  exiting from the RED unit have different concentration values for the current and future

377  scenarios, respectively. Conversely, the two solutions entering the regeneration unit have

378  similar concentration values for the current and future scenarios, due to the partial mixing

379  process required for the water-rebalancing.
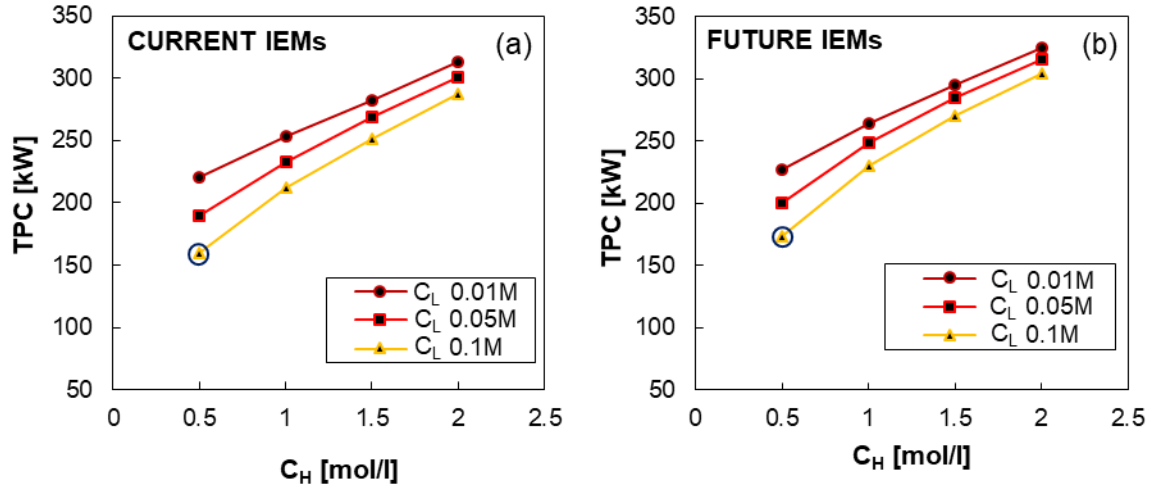
**Figure 6.** *Effect of inlet concentrations on TPC of the vapour stripping column for current (a) and future (b) scenarios. RED unit 1000 cell pairs 0.5x0.5 m², inlet velocities equal to 1 cm/s. $T_{waste-heat}$=80 °C. Blue circle is used to highlight the conditions for the best performance.*

The ratio between the gross power output of the RED unit and the TPC of the regeneration unit is the thermal efficiency. Figure 7 shows the effect of inlet concentration on the thermal and exergy efficiencies for current (a) and future membranes (b). In both cases, the highest efficiency is achieved for the highest driving force (2 M-0.01 M) because the salinity gradient affects the power production more than TPC. As a matter of fact, considering the current scenario and $C_L$=0.01 M, an increase of the concentration of the high solution from 0.5 M to 2 M doubles the power density from 1 W/m² to 2 W/m², while the thermal energy consumption inc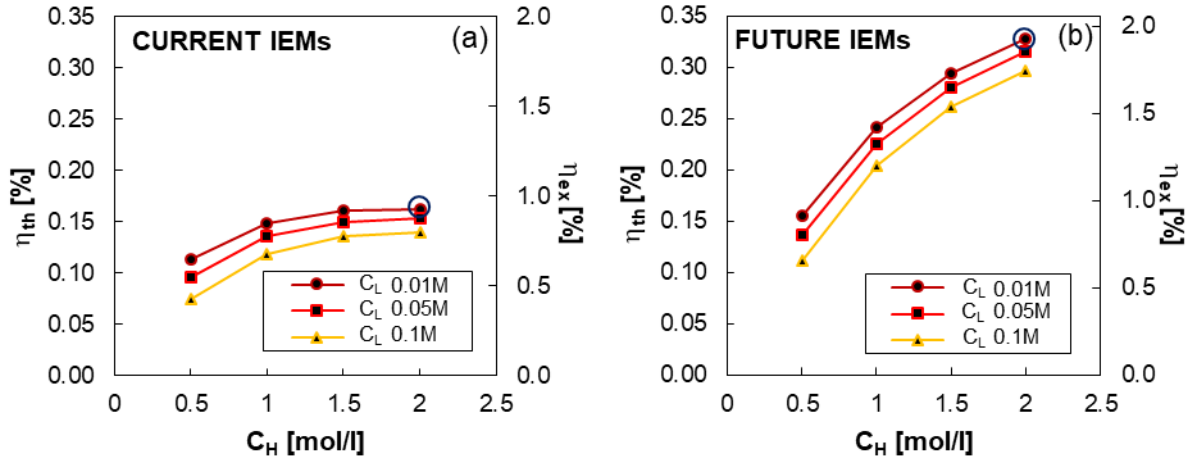reases about 50%. This effect is more marked in the future scenario where the power density is increased almost three times (i.e., from 1.5 W/m² to 4.25 W/m²), while the power consumption is comparable to the one in the current scenario. As result, the highest thermal efficiency in the current scenario is equal to 0.16% ($\eta_{ex}$= 0.9%), while in the future scenario is equal to 0.32% ($\eta_{ex}$= 1.93%).

Figure 7. *Effect of the inlet concentrations on $\eta_{th}$ and $\eta_{ex}$ of the t-RED HE for current (a) and future (b) scenarios. RED unit 1000 cell pairs 0.5x0.5 m², inlet velocities equal to 1 cm/s. Blue circle is used to highlight the conditions of the best performance.*

## 3.2    Influence of inlet velocities on the system performance

The following sensitivity analyses concern the effect of the inlet solution velocities on the main performance parameters of the t-RED HE, fixing the inlet concentration of the two solutions in the RED unit to the values that provided the highest efficiency in the previous analysis (i.e., $C_H$=2 M and $C_L$=0.01 M).

The influence of the feed inlet velocities on $P_{d,max}$ is reported in Figure 8. As expected, the gross power density is a growing function of the solution velocities. In particular, $P_{d,max}$ is affected by the dilute velocity, while only slight variations are observed with the concentrate velocity. The highest $P_{d,max}$ is equal to 2.6 W/m² in the current scenario. Due to the membrane improvements, $P_{d,max}$ in the future scenario is more than double of the current one, i.e., 5.7 W/m².
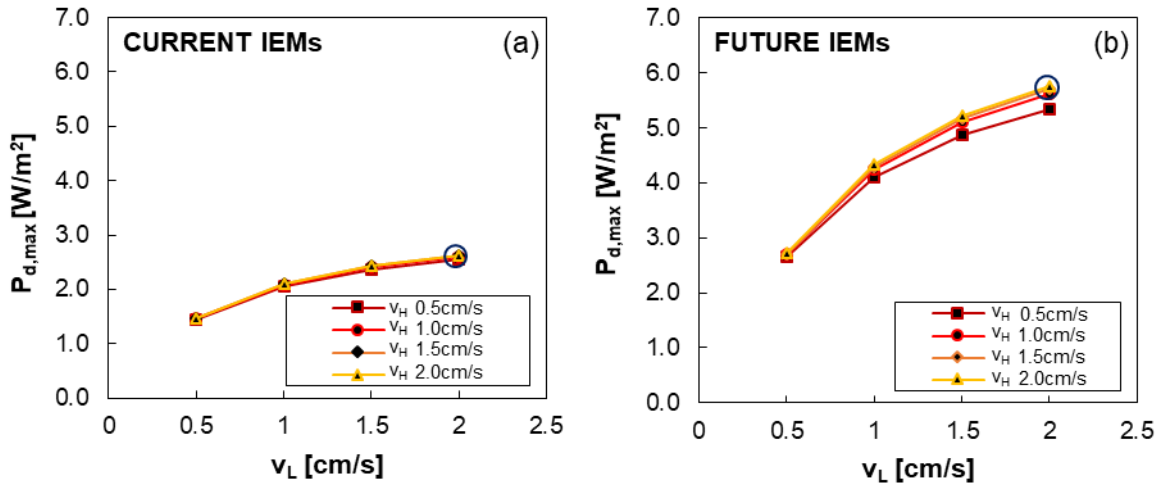
**Figure 8.** *Effect of the inlet velocities on $P_{d,max}$ of the RED unit for current (a) and future (b) scenarios. RED unit 1000 cell pairs 0.5x0.5 $m^2$, inlet concentrations equal to $C_H=2$ M and $C_L=0.01$ M. Blue circle is used to highlight the conditions of the best performance.*

The influence of RED inlet velocities on the TPC of the vapour stripping column is reported in Figure 9a and 9b for current and future membranes, respectively. TPC linearly increases with the dilute flow rate. The higher the dilute flow rate fed to the stripping column, the higher the amount of stripping vapour that is required in the regeneration unit. TPC is slightly affected by the velocity of the concentrate and the adoption of either current or future membranes. The lowest TPC of about 180 kW is observed in the case of dilute inlet velocities of 0.5 cm/s.
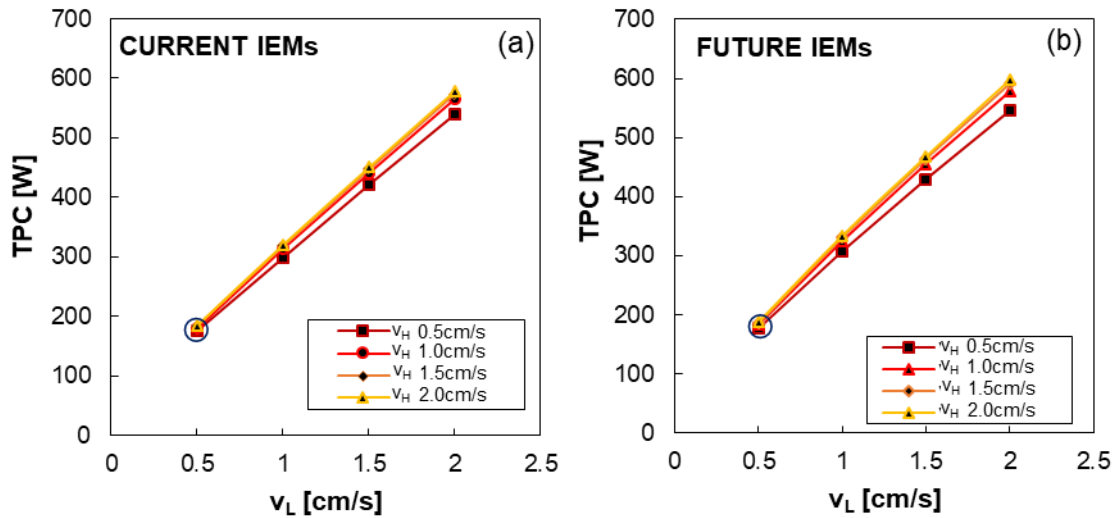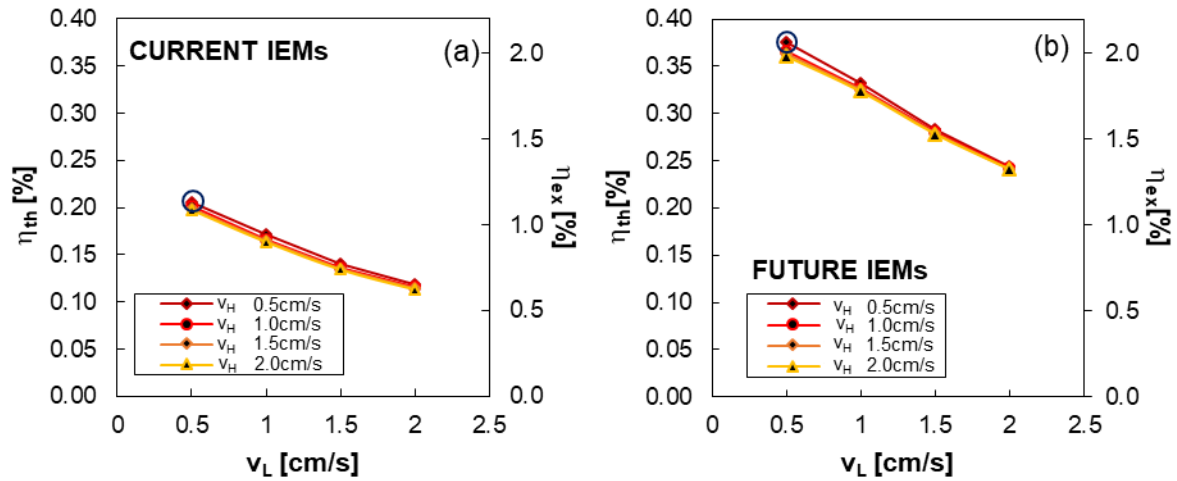
**Figure 9.** *Effect of the inlet velocities on TPC of the vapour stripping column for current (a) and future (b) scenarios. RED unit 1000 cell pairs $0.5 \times 0.5 m^2$, inlet concentrations equal to $C_H = 2$ M and $C_L = 0.01$ M. $T_{waste-heat} = 80$ °C. Blue circle is used to highlight the conditions of the best performance.*

The effect of RED inlet velocities on the thermal and exergy efficiencies of the whole t-RED HE is depicted in Figure 10a and 10b for current and future membranes, respectively. In both current and future scenarios, the unit efficiency is dominated by the influence of the velocities on TPC. Thus, the maximum efficiency is obtained for the lowest TPC, which is observed at the lowest inlet velocities (i.e., $v_H = v_L = 0.5$ cm/s). The highest thermal efficiency in the current scenario is equal to 0.2%, which corresponds to an exergy efficiency of 1.1%. In the case of future enhanced membranes, the thermal efficiency increases up to 0.36% while the exergy efficiency reaches values around 2.10%.

**Figure 10.** *Effect of inlet velocities on $\eta_{th}$ and $\eta_{ex}$ of the t-RED HE for current (a) and future (b) scenarios. RED unit 1000 cell pairs 0.5x0.5 $m^2$, inlet concentrations equal to $C_H=2$ M and $C_L=0.01$ M. Single. $T_{waste-heat}=80$ °C. Blue circle is used to highlight the conditions of the best performance.*

## 3.3    Multi-stage regeneration unit

The previous sensitivity analyses on the t-RED HE has highlighted that in all the investigated conditions, the high thermal consumption of the vapour stripping column is the limiting factor, which leads to low efficiency values also in the case of future enhanced membranes. The high thermal power consumption is caused by the partial vaporization of the solution in the reboiler to generate the stripping steam. However, only a small part of the thermal energy contained in this stream is used to strip the gas. As a result, most of the heat that is supplied remains in the vapour steam exiting from the top of the column and it is discharged in the condensation step (see condenser in *Figure 3*). In order to increase the energetic efficiency of the regeneration unit, this heat should be recovered and reused within the unit.

A possible alternative already proposed in the literature [30] for forward osmosis applications is to exploit the enthalpy of vaporization remaining in the stripping gas as an energy source for a following stripping column operating at lower pressure. In this way, a multi-column configuration is obtained, similarly to a MED unit. When a multi-column system is considered,

23

454    the solution exiting from mixer 1 (Figure 11) is split and fed in parallel to the stripping columns.

455    Only the heat supplied in the first column is coming from an external source (i.e., waste heat),

456    while the following columns are fed by the heat obtained from vapour condensation of the

457    previous column as shown in Figure 11. The absorption step operates in the same way for both

458    single and multi-stage processes as the amount of gases stripped in the two different

459    configurations remains practically the same.

460    Differently from the MED process, where a large number of effects can be adopted to increase

461    the thermal efficiency of the process, in the present case of a multi-column arrangement, the

462    number of columns or stages is limited due to the multi-component nature of the condensing

463    vapour. Indeed, the condensation process takes place in a range of condensation temperatures

464    between 4-8 °C, consuming rapidly the available temperature difference between the first and

465    the last columns, and resulting in a small number of units. As an example, fixing the top

466    temperature at 80 °C and the lowest operating pressure equal to 0.05 bar (i.e. bottom

467    temperature around 30 °C), the maximum number of columns is equal to 5.



468
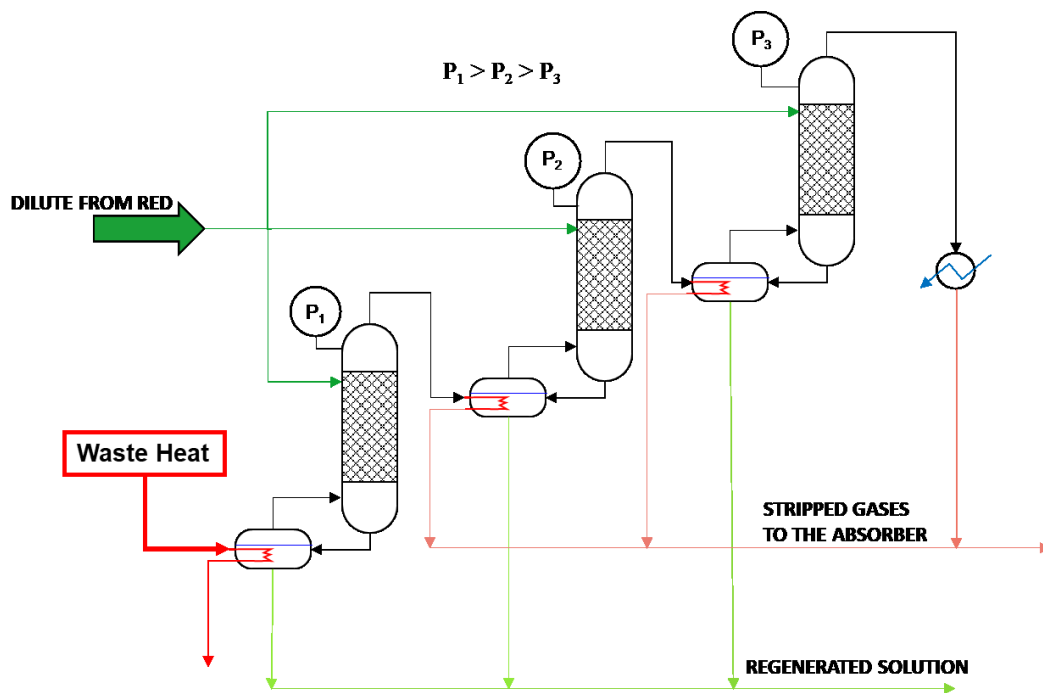
469    ***Figure 11.*** *Schematic representation of a three stages vapour stripping column.*

470

471     The thermal and exergy efficiencies of the t-RED HE fed by waste heat at 80°C as a function

472     of the number of columns in series, are reported in Figure 12. Operating conditions at the RED

473     unit inlet (i.e., concentration and velocity of solutions) were fixed equal to those of the previous

474     sections 3.1 and 3.2, which led to the highest efficiency (i.e., $C_H$ = 2 M $C_L$ = 0.01 M $v_H$ = $v_L$ =

475     0.5 cm/s). The efficiency increase is not a linear function of the number of stripping columns.

476     In fact, the efficiency is more than doubled when shifting from 1 to 2 columns (from $\eta_{ex,1}$ =

477     1.3% to $\eta_{ex,2}$ =2.7%), while it is only four times higher in the case of 5 columns in series

478     ($\eta_{ex,5}$=5.1%). In the future scenario, using a 5-column configuration the thermal and exergy

479     efficiencies are equal to 1.4% and 8.5%, respectively.
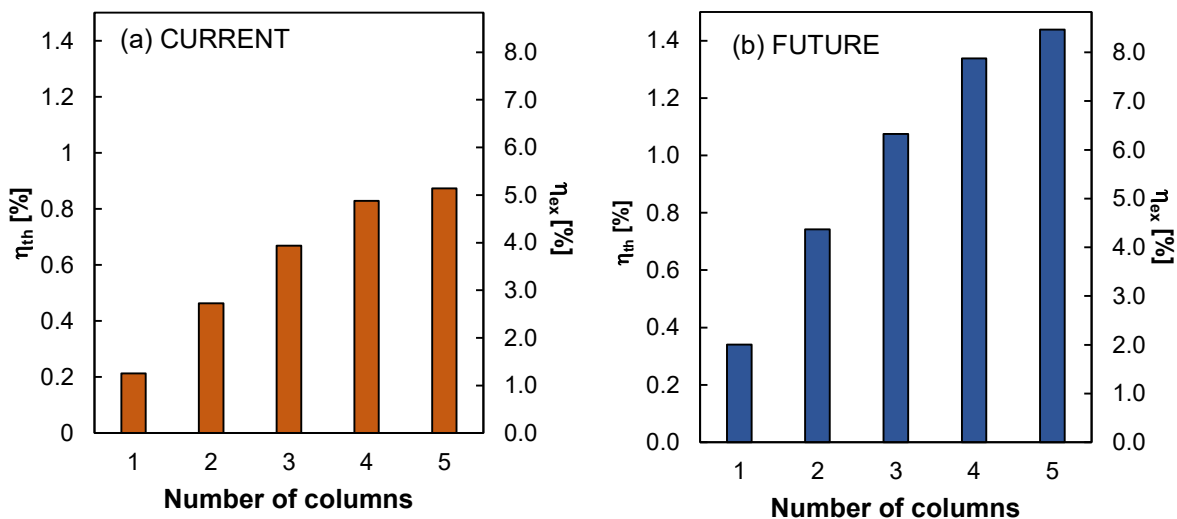


480

481     *Figure 12. Thermal and exergy efficiencies of the t-RED HE as a function of the number of stripping*

482     *column adopted in the regeneration unit for current (a) and future (b) membranes. RED unit 1000 cell*

483     *pairs 0.5x0.5 m², $v_H$= $v_L$=0.5 cm/s, $C_H$=2 M, $C_L$=0.01 M. $T_{waste-heat}$=80 °C, $T_{last,column}$=30 °C.*

484     Interestingly, the temperature of the waste heat fed into the first reboiler determines the number

485     of stripping units placed in series. The lower the waste heat temperature, the less stripping

486     columns can be used and thus the lower the thermal efficiency. In this work, the temperature of

487     waste heat was fixed at 80 °C, as any further temperature increase has been proven to generate

488     a negligible efficiency increase of the multi-column system. However, the increase of waste

489  heat temperature can be useful to increase the temperature driving force for heat exchange in

490  the reboilers, thus reducing the heat exchanger area and the relevant capital cost.

491  **4   CONCLUSIONS**

492  In this work, an experimentally validated model was developed to analyse the performance of

493  the t-RED HE varying the operating conditions and considering (i) a current scenario where

494  commercial membranes (i.e., Fujifilm Type 10 membranes) are used and (ii) a future scenario

495  where enhanced membrane properties are adopted. The highest exergy efficiency achieved in

496  the current scenario is equal to 1.25% while in the future scenario it is equal to ~2%.

497  Higher efficiencies can be reached by adopting a multi-stage regeneration unit due to the

498  increase of the thermal efficiency of the regeneration, achieving a better exploitation of the

499  external waste heat. The exergy efficiency of the system is increased from 1.25% to 5.2% when

500  using 5 columns. A further increase up to 8.5% is obtainable considering enhanced future

501  membranes.

502  This novel heat engine converts very low-grade heat (e.g. below 100°C) into power. However,

503  the efficiencies found are low thus suggesting the need for further improvements. The use of

504  alternative solvent-solute couples or even the adoption of salt mixtures should be investigated

505  in the future, in order to find more efficient solutions.

506  Achieving higher efficiency values at acceptable costs would guarantee the recovery of large

507  amounts of waste heat available at low temperature levels which the RED HE is able to convert.

508  This would allow industrial power plants to increase their efficiency and sustainability by

509  reducing the energy costs and the carbon dioxide emissions.

510

511 **ACKNOWLEDGEMENTS**

515     **NOMENCLATURE**

| | |
|---|---|
| $A_{cp}$ | cell pair membrane area (m$^2$) |
| $b$ | membrane width (m) |
| $C_H$ | concentrate molar concentration (M) |
| $C_L$ | dilute molar concentration (M) |
| $E_{cell}$ | voltage generated by the cell pair (V) |
| $E_{stack}$ | voltage generated by the pile (V) |
| $F$ | Faraday constant (C/mol) |
| $i(k)$ | electric current of the generic $k^{th}$ element |
| $I_{stack}$ | total Electric current (A) |
| $m$ | molality (mol/kg$_{solv}$) |
| $M1$ | mixer 1 |
| $M2$ | mixer 2 |
| $MW_s$ | salt Molecular weight (kg/mol) |
| $N_{cp}$ | number of cell pair |
| $N_k$ | number of discretization elements |
| $P_d$ | power density (W/m$^2$) |
| $P_{d,max}$ | maximum power density (W/m$^2$) |
| $P_{loss}$ | pumping power required (W) |
| $P_{RED}$ | electric power outputs from the RED unit (W) |
| $Q$ | volumetric flow rate (m$^3$/s) |
| $R$ | universal gas constant (J/(K mol)) |
| $R_{AEM}$ | anionic membrane resistance ($\Omega$m$^2$) |
| $R_{blamk}$ | electrical resistance of the electrodic compartment ($\Omega$) |
| $R_{cell}$ | electrical resistance of the cell pair ($\Omega$) |

| $R_{CEM}$ | cationic membrane resistance ($\Omega m^2$) |
|---|---|
| $R_E$ | load resistance ($\Omega$) |
| $R_H$ | electrical resistance of concentrate ($\Omega m^2$) |
| $R_{IEM,av}$ | average ionic exchange membrane resistance ($\Omega m^2$) |
| $R_L$ | electrical resistance of dilute ($\Omega m^2$) |
| $T$ | temperature (°C or K) |
| $TPC$ | thermal power consumption (W) |
| v | solution velocity (m/s) |
| $z$ | valence of the ions |

## Greek symbols

| $\alpha_{av}$ | average ionic exchange membrane permselectivity |
|---|---|
| $\Delta x$ | calculation element length (m) |
| $\eta_C$ | Carnot efficiency |
| $\eta_{ex}$ | exergy efficiency |
| $\eta_{th}$ | thermal efficiency |
| $\gamma$ | salt activity coefficient (dimensionless) |
| $\rho$ | density (kg/m³) |

## Subscripts

| gross | related to gross value |
|---|---|
| H | related to the concentrate stream |
| H-mix1 | related to the part of the outlet concentration fed to the mix1 |
| in | related to the inlet solution from RED unit |
| L | related to the dilute stream |
| mix1 | related to the outlet solution from mixer 1 |
| net | related to net consumptions |
| out | related to the outlet solution from RED unit |
| HOT | related to the hot reservoir |
| COLD | related to the cold reservoir |
| waste-heat | related to the waste heat |

## Acronyms

| | |
|---|---|
| E-NRTL-RK | Electrolyte Non Random Two Liquid Redlich-Kwong |
| HE | Heat Engine |
| IEM | Ionic Exchange Membrane |
| MD | Membrane Distillation |
| MED | Multi Effect Distillation |
| PRO | Pressure Retarded Osmosis |
| PRO-MD HE | Pressure Retarded Osmosis Membrane Distillation Heat Engines |
| RED | Reverse Electrodialysis |
| RED HE | Reverse ElectroDialysis Heat Engine |
| SGP | Salinity Gradient Power |
| SGP HE | Salinity Gradient Power Heat Engines |
| t-RED HE | Thermolytic Reverse ElectroDialysis Heat Engine |

516

## REFERENCES

518  [1]    A. Tamburini, M. Tedesco, A. Cipollina, G. Micale, M. Ciofalo, M. Papapetrou, W. Van Baak,
519         A. Piacentino, Reverse electrodialysis heat engine for sustainable power production, Appl.
520         Energy. 206 (2017) 1334–1353. doi:10.1016/j.apenergy.2017.10.008.

521  [2]    M. Papapetrou, G. Kosmadakis, A. Cipollina, U. LaCommare, G. Micalea, Industrial waste heat:
522         Estimation of the technically available resource in the EU per industrial sector, temperature level
523         and      country,     Appl.     Therm.     Eng.     138     (2018)     207–216.
524         doi:10.1016/j.applthermaleng.2018.04.043.

525  [3]    B.E. Logan, M. Elimelech, Membrane-based processes for sustainable power generation using
526         water, Nature. 488 (2012) 313–319. doi:10.1038/nature11477.

527  [4]    S. Loeb, Method and apparatus for generating power utilizing Pressure-Retarded-Osmosis, US
528         Patent 3906250, 1974.

529  [5]    S. Loeb, Method and apparatus for generating power utilizing Reverse Electrodialysis, US Patent
530         4171409, 1978.

531  [6]    S. Lin, N.Y. Yip, T.Y. Cath, C.O. Osuji, M. Elimelech, Hybrid Pressure Retarded Osmosis–

Membrane Distillation System for Power Generation from Low-Grade Heat: Thermodynamic Analysis and Energy Efficiency, Environ. Sci. Technol. 48 (2014) 5306–5313. doi:10.1021/es405173b.

[7]   R. Long, B. Li, Z. Liu, W. Liu, Hybrid membrane distillation-reverse electrodialysis electricity generation system to harvest low-grade thermal energy, J. Memb. Sci. 525 (2017) 107–115. doi:10.1016/j.memsci.2016.10.035.

[8]   M. Micari, A. Cipollina, F. Giacalone, G. Kosmadakis, M. Papapetrou, G. Zaragoza, G. Micale, A. Tamburini, Towards the first proof of the concept of a Reverse ElectroDialysis - Membrane Distillation Heat Engine, Desalination. 453 (2019) 77–88. doi:10.1016/j.desal.2018.11.022.

[9]   J. Hu, S. Xu, X. Wu, D. Wu, D. Jin, P. Wang, Q. Leng, Theoretical simulation and evaluation for the performance of the hybrid multi-e ff ect distillation — reverse electrodialysis power generation system, 443 (2018) 172–183. doi:10.1016/j.desal.2018.06.001.

[10]  P. Palenzuela, M. Micari, B. Ortega-Delgado, F. Giacalone, G. Zaragoza, D.-C. Alarcón-Padilla, A. Cipollina, A. Tamburini, G. Micale, Performance Analysis of a RED-MED Salinity Gradient Heat Engine, Energies. 11 (2018) 3385. doi:10.3390/en11123385.

[11]  E. Shaulsky, C. Boo, S. Lin, M. Elimelech, Membrane-based osmotic heat engine with organic solvent for enhanced power generation from low-grade heat, Environ. Sci. Technol. 49 (2015) 5820–5827. doi:10.1021/es506347j.

[12]  M. Marino, L. Misuri, A. Carati, D. Brogioli, Proof-of-concept of a zinc-silver battery for the extraction of energy from a concentration difference, Energies. 7 (2014) 3664–3683. doi:10.3390/en7063664.

[13]  K.L. Hickenbottom, J. Vanneste, T.Y. Cath, Assessment of alternative draw solutions for optimized performance of a closed-loop osmotic heat engine, J. Memb. Sci. 504 (2016) 162–175. doi:10.1016/j.memsci.2016.01.001.

[14]  A. Carati, M. Marino, D. Brogioli, Thermodynamic study of a distiller-electrochemical cell system for energy production from low temperature heat sources, Energy. 93 (2015) 984–993. doi:10.1016/j.energy.2015.09.108.

[15]  F. Giacalone, C. Olkis, G. Santori, A. Cipollina, S. Brandani, G. Micale, Novel solutions for

560       closed-loop reverse electrodialysis: Thermodynamic characterisation and perspective analysis,

561       Energy. 166 (2019) 674–689. doi:10.1016/j.energy.2018.10.049.

562    [16]    M. Micari, M. Bevacqua, A. Cipollina, A. Tamburini, W. Van Baak, T. Putts, G. Micale, Effect

563       of different aqueous solutions of pure salts and salt mixtures in reverse electrodialysis systems

564       for closed-loop applications, J. Memb. Sci. 551 (2018) 315–325.

565       doi:10.1016/j.memsci.2018.01.036.

566    [17]    R.L. McGinnis, J.R. McCutcheon, M. Elimelech, A novel ammonia–carbon dioxide osmotic heat

567       engine for power generation, J. Memb. Sci. 305 (2007) 13–19.

568       doi:10.1016/j.memsci.2007.08.027.

569    [18]    X. Luo, X. Cao, Y. Mo, K. Xiao, X. Zhang, P. Liang, X. Huang, Power generation by coupling

570       reverse electrodialysis and ammonium bicarbonate: Implication for recovery of waste heat,

571       Electrochem. Commun. 19 (2012) 25–28. doi:10.1016/j.elecom.2012.03.004.

572    [19]    R.D. Cusick, Y. Kim, B.E. Logan, Energy Capture from Thermolytic Solutions in Microbial

573       Reverse-Electrodialysis Cells, Science (80-. ). 335 (2012) 1474–1477.

574       doi:10.1126/science.1219330.

575    [20]    K. Kwon, B.H. Park, D.H. Kim, D. Kim, Parametric study of reverse electrodialysis using

576       ammonium bicarbonate solution for low-grade waste heat recovery, Energy Convers. Manag.

577       103 (2015) 104–110. doi:10.1016/j.enconman.2015.06.051.

578    [21]    M. Bevacqua, A. Carubia, A. Cipollina, A. Tamburini, M. Tedesco, G. Micale, Performance of

579       a RED system with ammonium hydrogen carbonate solutions, Desalin. Water Treat. 57 (2016)

580       23007–23018. doi:10.1080/19443994.2015.1126410.

581    [22]    D.H. Kim, B.H. Park, K. Kwon, L. Li, D. Kim, Modeling of power generation with thermolytic

582       reverse electrodialysis for low-grade waste heat recovery, Appl. Energy. 189 (2017) 201–210.

583       doi:10.1016/j.apenergy.2016.10.060.

584    [23]    M. Bevacqua, A. Tamburini, M. Papapetrou, A. Cipollina, G. Micale, A. Piacentino, Reverse

585       electrodialysis with NH4HCO3-water systems for heat-to-power conversion, Energy. 137 (2017)

586       1293–1307. doi:10.1016/j.energy.2017.07.012.

587    [24]    F. Giacalone, P. Catrini, A. Tamburini, A. Cipollina, A. Piacentino, G. Micale, Exergy analysis

588      of reverse electrodialysis, Energy Convers. Manag. 164 (2018) 588–602.
589      doi:10.1016/j.enconman.2018.03.014.

590  [25]  T.Z. Fahidy, Activity coefficients in electrolyte solutions (second edition), edited by Kenneth S.
591      Pitzer, 1991, 542 + vi pages, CRC Press, Boca Raton, FL; ISBN 0-8493-5415-3. Price: US$
592      195.00, Can. J. Chem. Eng. 71 (1993) 494–494. doi:10.1002/cjce.5450710328.

593  [26]  E.I. Rashkovskaya, E.A.; Chernen'kaya, Densities of ammonium bicarbonate, sodium
594      bicarbonate, and ammonium chloride and ammonia salt solutions at 20-100°C, Zhurnal Prikl.
595      Khimii. 40 (1967) 301.

596  [27]  G. Jones, C.F. Bickford, The Conductance of Aqueous Solutions as a Function of the
597      Concentration. I. Potassium Bromide and Lanthanum Chloride, J. Am. Chem. Soc. 56 (1934)
598      602–611. doi:10.1021/ja01318a021.

599  [28]  R. Ashu, S. Pawlowski, J. Veerman, K. Bouzek, E. Fontananova, S. Velizarov, J. Goulão, K.
600      Nijmeijer, E. Curcio, Progress and prospects in reverse electrodialysis for salinity gradient
601      energy conversion and storage, 225 (2018) 290–331. doi:10.1016/j.apenergy.2018.04.111.

602  [29]  A. Tamburini, A. Cipollina, M. Papapetrou, A. Piacentino, G. Micale, 7 – Salinity gradient
603      engines, in: Sustain. Energy from Salin. Gradients, 2016: pp. 219–256. doi:10.1016/B978-0-08-
604      100312-1.00007-9.

605  [30]  R.L. McGinnis, M. Elimelech, Energy requirements of ammonia–carbon dioxide forward
606      osmosis desalination, Desalination. 207 (2007) 370–382. doi:10.1016/j.desal.2006.08.012.

607  [31]  EU, RED-Heat-to-Power, (2015). www.red-heat-to-power.eu. (accessed February 22, 2019).

608  [32]  T.Z. Fahidy, Activity coefficients in electrolyte solutions (second edition), edited by Kenneth S.
609      Pitzer, 1991, 542 + vi pages, CRC Press, Boca Raton, FL; ISBN 0-8493-5415-3. Price: US$
610      195.00, Can. J. Chem. Eng. 71 (1993) 494–494. doi:10.1002/cjce.5450710328.

611  [33]  Z. Meng, J.H. Seinfeld, P. Saxena, Y.P. Kim, Atmospheric Gas-Aerosol Equilibrium: IV.
612      Thermodynamics of Carbonates, Aerosol Sci. Technol. 23 (1995) 131–154.
613      doi:10.1080/02786829508965300.

614

615

**APPENDIX**

**A.1.**          **Ammonium bicarbonate-water solution properties**

*Osmotic and mean activity coefficients of ammonium bicarbonate-water solutions*

Pitzer's ion interaction model [32] was used to evaluate the osmotic and activity coefficients of NH$_4$HCO$_3$-water solutions. In Pitzer's equation the osmotic and mean activity coefficients are expressed as function of the solution molality through fitting coefficients, named virial coefficients, which account for the interactions between the ions.

$$\varphi = 1 - |z_M z_X| A_\varphi \frac{I^{0.5}}{1 + bI^{0.5}} + 2m \frac{\nu_M \nu_X}{\nu} B_{MX}^\varphi + 2m^2 \frac{(\nu_M \nu_X)^{3/2}}{\nu} C_{MX}^\varphi \tag{A.1}$$

$$\ln(\gamma_\pm) = -|z_M z_X| A_\varphi \left( \frac{I^{0.5}}{1 + bI^{0.5}} + \frac{2}{b} \ln(1 + bI^{0.5}) \right) + 2m \frac{\nu_M \nu_X}{\nu} B_{MX}^\gamma + 3m^2 \frac{(\nu_M \nu_X)^{3/2}}{\nu} C_{MX}^\varphi \tag{A2}$$

With

$$B_{MX}^\varphi = B_{MX}^{(o)} + B_{MX}^{(1)} \exp(-\alpha I^{0.5}) \tag{A.3}$$

$$B_{MX}^\gamma = 2B_{MX}^{(o)} + \frac{2B_{MX}^{(1)}}{\alpha^2 I} \left[ 1 - (1 + \alpha I^{0.5} - \frac{\alpha^2 I}{2}) \exp(-\alpha I^{0.5}) \right] \tag{A.4}$$

where $m_0 = 1$ mol·kg$^{-1}$ is the standard molality, $b = 1.2$ kg$^{1/2}$mol$^{-1/2}$ is a universal parameter; $\alpha$ is a numerical constant equal to 2 for univalent ions; $I$ is the ionic strength $A_\phi$, is the Debye-Huckel parameter for the osmotic coefficient; $z_M$ and $z_X$ are the charges of cation and anion; $B^{(0)}{}_{MX}$, $B^{(1)}{}_{MX}$, and $C_{MX}$ are the *ion-interaction parameters or virial coefficients*. The virial coefficients for NH$_4$HCO$_3$ solutions at 298°K are reported in [33]. The behaviour of osmotic and activity coefficients as function of solution molality at 298°K is reported in Figure A. 1.

**NH₄HCO₃-water solutions**

634
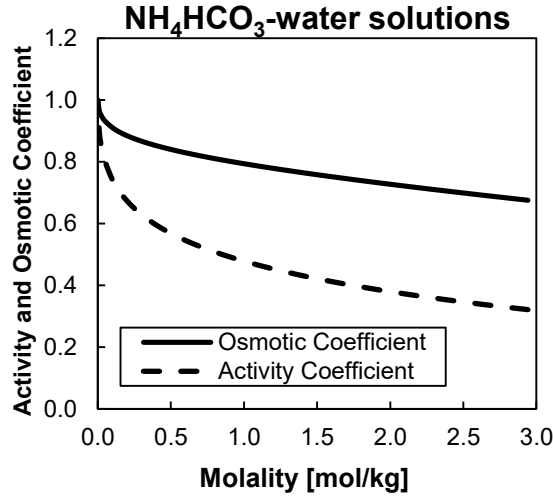
**Figure A. 1.** *Osmotic and salt activity coefficients for NH₄HCO₃-water solution at 298.15 K as*

*function of molality. Pitzer's coefficients from* [33].

*Density of ammonium bicarbonate-water solutions*

The NH₄HCO₃-water density was evaluated as a linear function of the molar concentration as:

$$\rho = \rho_0 + \left(\frac{\Delta\rho}{\Delta C}\right) C \qquad (A.5)$$

where $\rho_0$ is density of pure water at 298.15 K, which is equal to 997 kg/m³. The slope of the function

$(\Delta\rho/\Delta C)$ was evaluated by fitting experimental data from literature [26]. In the case of NH₄HCO₃-

water solution, $\Delta\rho/\Delta C$ is equal to 35.53 kg/mol. Figure A.2a shows the density of NH₄HCO₃-

water solution as function of the molar concentration. As it can be seen a good fitting was found.

*Conductivity of ammonium bicarbonate-water solutions*

The conductivity of NH₄HCO₃-water solutions as function of solution molarity is computed

according to Eq. A.6 [27].

$$\Lambda = \Lambda_0 - \frac{A_\Lambda C^{1/2}}{1 + B_\Lambda C^{1/2}} - C_\Lambda C \qquad (A.6)$$

where $\Lambda_0$ is the equivalent conductivity of salt at infinite dilution, $A_\Lambda$, $B_\Lambda$ and $C_\Lambda$ are fitting

parameters, and $C$ is the molar concentration. The parameters of equation A.6 for NH₄HCO₃-

water solutions, obtained by fitting of experimental data are $A_\Lambda=30.32$, $B_\Lambda=0$ and $C_\Lambda=0$. The

651    dependence of conductivity on the concentration for $NH_4HCO_3$ aqueous solutions is reported

652    in Figure A.2b, where the soundness of the correlation can be also observed.
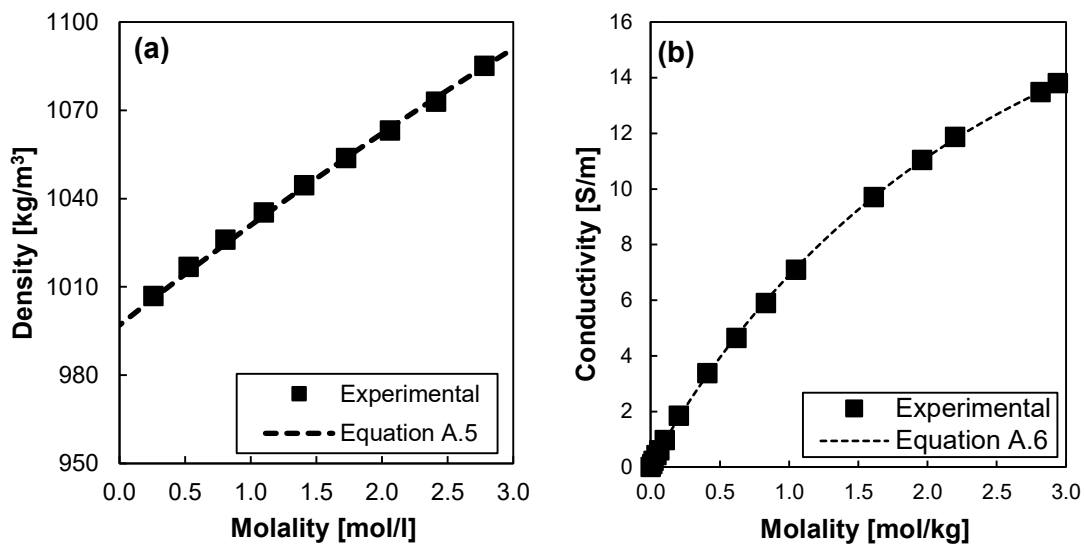


653

654    **Figure A.2.** *Comparison of experimental and fitting results of density (a) and conductivity (b) for*

655    *$NH_4HCO_3$ aqueous solutions as function of molarity at 298.15 K.*

656